How Important Is the Spectral Ripening Effect in Stratiform Boundary Layer Clouds? Studies Using Simple Trajectory Analysis

R. WOOD

Met Office, Bracknell, Berkshire, United Kingdom

S. IRONS AND P. R. JONAS

Physics Department, University of Manchester Institute of Science and Technology, Manchester, United Kingdom

(Manuscript received 15 March 2001, in final form 14 February 2002)

ABSTRACT

Any population of cloud droplets forming on polydisperse condensation nuclei is thermodynamically unstable. There is no value of the supersaturation for which the growth rate of all the droplets is zero, so that if some droplets are in equilibrium, then some must have positive and some negative growth rates. Droplets with positive growth rates will continue to grow at the expense of those with negative growth rates. This effect has been termed the ripening process, and has been postulated to be a potential mechanism to explain broad droplet size distributions in stratiform clouds. In this paper multiple parcel trajectories are used, derived using a simple representation of the turbulent dynamics, to examine the time evolution of the droplet size distribution in a nonentraining stratiform cloud. It is shown that the magnitude of the effect is critically dependent upon the mean parcel in-cloud residence time. The simulations suggest that, for a stratiform clouds of $h = 400$ m thickness, and a vertical wind standard deviation of $\sigma_w = 0.6$ m s^{-1} (typical for stratocumulus clouds in a fairly vigorous, well-mixed boundary layer), the ripening effect is negligible, in that the droplet size distribution changes little with time. However, clouds with low $\sigma_w = 0.2$ m s^{-1} (typical of weaker stratus clouds) show a marked spectral ripening effect over a period of several hours. Ripening is observed in the numerical model in both clean and polluted aerosol distributions. Autoconversion rates calculated from the droplet size distributions increase markedly with time as ripening takes place. It is suggested that to accurately model droplet size distributions in stratus cloud, it may be necessary to take into account the distribution of in-cloud parcel residence time.

1. Introduction

The problem of modeling droplet size distributions in stratiform boundary layer cloud has been the focus of research efforts for over 50 years. The reasons why the droplet size distribution is so crucial to our understanding of cloud processes justify the considerable expense incurred: both cloud optical properties (Stephens 1978) and warm rain formation (see the review of Beard and Ochs 1993) are strongly determined by the partitioning of liquid water content among droplets of different sizes.

Single adiabatic parcel model ascents have provided key insights into the processes occurring to hydrophilic aerosol as they pass from subsaturated to supersaturated air (e.g., Howell 1949). Comparison between modeled and observations size distributions (Fitzgerald 1972) suggested that droplet size distributions within warm clouds are significantly broader than those modeled using a single adiabatic ascent. Subsequent improvements to observational capability have confirmed the generality of this result (e.g., Brenguier and Chaumat 2001). The workhorse of the cloud droplet measurement community is the Forward Scattering Spectrometer Probe (FSSP, Particle Measuring Systems, Inc.). This instrument has been subject to a great deal of scrutiny in an attempt to validate its accuracy in counting and sizing cloud droplets (Dye and Baumgardner 1984; Baumgardner et al. 1985; Wendisch et al. 1996; Brenguier et al. 1998). There is a general consensus that droplet size distributions measured with the FSSP are artificially broadened by a number of instrumental effects including coincidence oversizing (measurement of two or more small droplets coincident in the laser beam as one larger droplet; e.g., Baumgardner et al. 1985). However, although taking into account artificial broadening effects has shown a reduction in the breadth of the measured droplet size distributions, it is not sufficient to generate agreement between measured and modeled distributions. Thus there remains a need for improved modeling methods to explain droplet size distribution breadth in warm clouds.

Corresponding author address: R. Wood, Department of Atmospheric Sciences, Box 351640, University of Washington, Seattle, WA 98102.
E-mail: robwood@atmos.washington.edu

Recent modeling efforts (Celik and Marwitz 1999, henceforth CM99) have shown that parcels of air that remain within a cloud for significant periods of time undergo a ripening process whereby large droplets can grow at the expense of smaller droplets. This has been termed ''Ostwald ripening,'' following pioneering observations of crystals in 1896 by W. Ostwald. Because larger droplets grow and smaller droplets shrink, the effect of this process is to broaden the spectrum at both small and large sizes. Srivastava (1991) demonstrates, using the droplet growth equation, that the difference between the squared radii of any two activated nuclei is expected to increase with time, rather than remain constant, if the effect of droplet surface tension is included. The droplet growth equation is written

$$r\frac{dr}{dt} = G(s - s_{eq}), \tag{1}$$

where r is the droplet radius; s is the supersaturation; s_{eq} is the equilibrium supersaturation, a function of the aerosol dry radius; and G is approximately constant at a particular temperature and pressure. Hence, for two activated nuclei (radii r_1 and r_2), ignoring s_{eq}, one can write

$$r_1\frac{dr_1}{dt} = r_2\frac{dr_2}{dt}, \tag{2}$$

so that the difference of the squared radii does not change with time. However, if the equilibrium supersaturation is not ignored, but instead the surface tension effect is retained, then this leads to a difference in squared radii that increases as time to some power α. To explain this, consider two activated droplets with different radii. Ignoring the solute effect, the larger of these droplets has a lower equilibrium supersaturation because the surface tension scales as r^{-1}. Therefore the rhs of Eq. (1) is larger for the larger droplet, and the difference in the square of the radius will increase with time. Following Srivastava (1991), this power α can be written as

$$\alpha \approx \text{const.} \times \frac{N}{w}, \tag{3}$$

where N is the total droplet concentration and w is the vertical ascent rate. Thus, the effect is greatest with (a) large droplet concentration, and (b) low updraft speeds. Using a single adiabatic parcel model, Srivastava (1991) shows how the variance of the droplet surface area distribution increases with time in a parcel ascent with a slow updraft (0.2 m s^{-1}), but that the increase becomes less important as the parcel ascent rate is increased. Korolev (1995) also demonstrated this effect in a cyclical parcel model and suggested that the broadening of the droplet size distributions is a consequence of an oscillating supersaturation field. However the simulations of CM99 show that, by imposing a sinusoidal in-cloud motion upon their parcel following its rise into cloud, the droplet size distributions are no broader than if the parcel remains at a constant height. This seems to suggest that the supersaturation fluctuations have little effect per se, and that the effect is predominantly governed by the residence time of the parcel in the cloud and the nature of the cloud condensation nuclei (CCN) supersaturation spectrum assumed. The results of Bartlett and Jonas (1972) demonstrate that a fluctuating updraft itself has little effect upon the spread of droplet sizes in an adiabatic parcel.

The major limitation of both the Korolev (1995) and CM99 studies in addressing the problem of spectral broadening in stratiform boundary layer clouds is that the in-cloud residence time of a parcel in real boundary layer clouds is a random variable, the probability density function (pdf) of which is a complicated function of the boundary layer dynamics and cloud geometry. In this study we attempt to use an ensemble of Lagrangian parcel trajectories subject to realistic turbulent motions within the boundary layer, to address the question of whether the ripening process is of consequence to the cloud droplet size distribution within stratus and stratocumulus clouds. Section 2 contains details of the ensemble model dynamics and microphysics; section 3 describes a set of numerical simulations to examine the hypothesis that the ripening process is important in stratus/stratocumulus clouds. Offline calculations of autoconversion from the model size distributions are presented in section 4. Finally, section 5 provides a discussion of the consequences of the findings.

2. Trajectory ensemble model (TEM) description and limitations

The evolution of the droplet size distribution is predicted using an ensemble of trajectories whose motion is driven by a stochastic model of realistic fluctuations in the boundary layer vertical wind field. The concept of the model and microphysical evolution is similar to that of Stevens et al. (1996) who forced a trajectory ensemble model using large eddy simulation (LES) dynamical fields. However, the trajectories in this case are all adiabatic (the effects of entrainment are not simulated) and are all initialized with the same total water mixing ratio and virtual potential temperature below cloud. There is no mixing between parcels. The simulations are intended to examine the effects of parcel in-cloud lifetime upon the droplet size distribution simply through the Ostwald ripening effect. Additional effects of extended parcel in-cloud residence time could potentially be introduced if radiative growth of droplets at the top of the cloud were included (e.g., Austin et al. 1995a; Harrington et al. 2000), but these are not examined here.

a. Dynamical evolution

To simulate the time evolution of the cloud droplet size distribution, an ensemble of one-dimensional parcel

trajectories is derived using the transilient matrix method (Nicholls 1987; Austin et al. 1995b). For the generation of trajectories, we relax the assumption that the parcels are mixed at each application of the transilient matrix so that the transilient matrix is then used only in the same way as a Langevin random walk model (De Baas et al. 1986) would be, that is, to derive parcel trajectories. The transilient model is perhaps easier to apply than the Langevin model because the impervious boundaries (surface and inversion) are automatically accounted for in the transilient model, whereas some specific treatment needs to be made in the Langevin approach. The transilient matrix elements are derived using the approach first introduced in Stull (1984), and further described in Austin et al. (1995b). Input parameters are vertical wind standard deviation σ_w and Lagrangian integral timescale τ_w. The assumption that the Eulerian and Lagrangian timescales are equal is assumed so that values of the Eulerian integral length scale (λ_w), as measured using horizontal traverses through cloud, can be used to constrain the trajectory properties. We use a 100-level domain and a time step of $\delta t_{\text{trans}} = 240$ s for generating the trajectories (i.e., parcel speed can change once every 240 s). Parcels are prevented from leaving the domain top (cloud top) and bottom (ground level). The Lagrangian integral timescales are derived from the resulting trajectory time series using the method of Lenschow and Stankov (1986), and are found to compare reasonably well with the desired ones (see appendix for more complete description of dynamical formulation). Later we show that the addition of realistic motions on timescales less than δt_{trans} makes little difference to the results in this study. Similarly, the results are not highly sensitive to changes in δt_{trans}.

b. Thermodynamic/microphysical evolution

For each simulation the trajectories are initialized at random levels below cloud base. No trajectories are initialized in the cloud as this would present difficulties in assigning liquid water content to different condensation nuclei. The pressure at each time step is calculated using the hydrostatic equation and the temperature along a trajectory is calculated using a standard adiabatic parcel with latent heat conversion. Cloud aerosol microphysics for each trajectory are computed from the droplet growth equation with kinetic corrections from Fukuta and Walter (1970; see also Pruppacher and Klett 1997) using a standard parcel model similar to that used in CM99. The number of aerosol categories used in all the simulations is $N = 60$ with logarithmic radius spacing. The smallest aerosol dry radius is $r_{\text{dry}} = 0.01$ μm, with dry aerosol mass doubling every two categories, giving a maximum dry size of just over 9 μm.

The hydrostatic equation, the temperature equation and the droplet growth equation are solved using a time step of $\delta t_{\text{micro}} = 0.1$ s along each Lagrangian trajectory. The supersaturation is calculated from the humidity mixing ratio, temperature, and pressure at each microphysical time step. The total moisture is a conserved variable and there is no ice. Finally, it is assumed that all aerosol particles consist entirely of ammonium sulfate. Because there is no droplet binning during the simulation, along each trajectory (in each parcel) there is a one-to-one mapping between the hydrated droplet radius and the dry aerosol radius. This mapping is lost only when size distributions are ''created'' in the postprocessing from the ensemble of trajectories.

c. Derivation of averaged quantities from the trajectory ensemble model

All binning is carried out after the runs have completed. Average droplet size distributions are calculated for particular time intervals and height intervals, using the complete set of trajectories. All simulations in this study contain $N_{\text{traj}} = 200$ trajectories. Thermodynamic, dynamic, and microphysical data are output once every δt_{trans} (=240 s) interval, and the total duration of the model runs was 200 min (50 s $\times$ 240 s). For trajectory heights distributed uniformly through the boundary layer, an average quantity would, in the mean, be constructed from $\overline{N}_{\text{contrib}} = N_{\text{traj}}(\delta z_{\text{ave}}/z_i)(\delta t_{\text{ave}}/\delta t_{\text{trans}})$ contributing quantities, where δz_{ave} is the height interval over which the average is to be taken, δt_{ave} is the averaging period, and z_i is the boundary layer depth. For height intervals of $\delta z_{\text{ave}} = 100$ m and averaging periods of $\delta t_{\text{ave}} = 40$ min (10 output steps), $N_{\text{contrib}} = 200$. The number of trajectories contributing to the average quantities can never exceed N_{traj}, but may be significantly less, because each trajectory has the potential to contribute up to $(\delta t_{\text{ave}}/\delta t_{\text{trans}})$ times to an average. Trajectories that have slow vertical ascent rates are likely to contribute more times per averaging period. That each trajectory can contribute more than once to an average should not be surprising: consider two aircraft runs through the same air space used to construct an arbitrary time–space average quantity. A parcel of air that remains at the level of the aircraft can be sampled twice in constructing the average.

The mean droplet size distribution in a particular time–height interval is binned into discrete haze–droplet size intervals. In this study there are 60 size bins, with the radii of the haze–droplet bins increasing by a factor of 10 every 20 bins.

d. Treatment of subcloud–cloud boundary

At relative humidities below cloud, hydrated haze particles are not sufficiently dilute to be grown using the standard growth equation. Growth/evaporation can become numerically unstable because of the rapid growth rates, and the behavior of concentrated salt solutions differs significantly from ideal solutions assumed in the derivation of the growth equation. We therefore assume that small haze particles ($r_{\text{dry}} < 1$ μm)

are in equilibrium with the parcel relative humidity when RH < 0.99 (lower than approximately 20 m below cloud base), and use the experimental results of Tang and Munkelwitz (1994) to calculate the humidity growth factor ($=r_{wet}/r_{dry}$) as a function of RH, where r_{dry} is the dry aerosol radius and r_{wet} is the equilibrium hydrated aerosol radius at RH. The shortest time taken for a parcel to travel a vertical distance of 20 m given realistic downdraft speeds is around 20 s. With RH $= 0.99$, droplets with radii less than approximately 4 μm evaporate to within 10% of their equilibrium radius within 20 s. It is therefore a reasonable assumption to treat $r_{dry} < 1$ μm haze particles as being in equilibrium. We allow larger haze particles to grow explicitly at all RH. It is not possible to do this with all the aerosol categories because of the numerical instabilities associated with high growth rates of small droplets. A comparison of runs where all RH < 0.99 is explicit ($r_{dry} > 1$ μm) with entirely equilibrium RH < 0.99 growth (for all r_{dry}), showed very little difference in the in-cloud droplet number and mass distributions. Just below cloud base ($0.95 <$ RH < 1.0) we found slightly higher concentrations (approximately 3%) of large haze particles ($r > 5$ μm) and slightly lower concentrations (approximately 4%) of small haze particles ($2 < r < 5$ μm) in the explicit growth run. This can be attributed to reduced evaporation rates for large haze particles in parcels descending through cloud base. It is concluded that the inclusion of explicit growth for $r_{dry} > 1$ μm particles below RH $= 0.99$ makes little difference to the in-cloud droplet size distributions.

e. Sensitivity tests

A number of approximations have been made in the derivation of the droplet growth equation. First, it has been assumed that the heat released by condensation of vapor onto a growing droplet is rapidly dissipated by conduction. It can be shown that this assumption of steady-state droplet minus environment temperature difference is a very good one apart from when the growing droplet radius is less than a factor of three larger than the dry aerosol radius. Because we have assumed that aerosols assume immediately their equilibrium size when the relative humidity drops below 0.99 (at which the aerosol growth factor for ammonium sulfate is approximately 3.6), we do not consider the explicit growth of drops smaller than around 3.5 times the radius of the dry aerosol, and so the effects of nonsteady-state temperature difference should not significantly affect the results [see, e.g., Pruppacher and Klett (1997) for a discussion on approximations to the droplet growth equation]. One set of model runs was performed with a time step $\delta t_{micro} = 0.01$ s, a factor of 10 less than that used in all the runs presented in this study, showed that there is very little sensitivity to the microphysical time step used. However, when the time step is increased to $\delta t_{micro} = 1$ s, it was found that some of droplets that formed on the smallest aerosol were activating even though the supersaturation was found not to exceed the critical supersaturation of the aerosol. This occurred even in low updrafts.

To examine the effects of small-scale turbulence upon the microphysical evolution we carried out two identical runs with and without turbulent vertical wind fluctuations on timescales smaller than the transilient time step δt_{trans}. We superimposed the fluctuations onto existing ($\delta t_{trans} = 240$ s) trajectories using a bounded cascade model fractional interpolator (Marshak et al. 1994; Cahalan et al. 1994) which gives Kolmogorov scaling down to the time step used for the droplet growth ($\delta t_{micro} = 0.1$ s). Further details of the method used to simulate small-scale turbulent fluctuations is given in the appendix. The addition of small-scale fluctuations is found to have negligible effect upon either the number or mass distributions.

f. Mixing timescales

An implicit assumption made in the simulations is that there is no interaction between individual parcels along the trajectories. It is impossible to account for parcel–parcel mixing in the current framework because each mixing ''event'' would generate additional degrees of freedom. Consider the mixing of two parcels, which have undergone no previous mixing (i.e., are described using N categories). To describe the droplet–aerosol system for the mixed parcel will require $2N$ categories because each parcel contains a different one-to-one mapping between wet and dry particle size. As the number of mixing events increases, the number of categories required increases as a geometric progression.

How long does it take for parcels to be completely mixed and lose their individual identities? One timescale, which has been shown to be an effective measure of the mixing timescale, is the Corrsin timescale τ_{mix} given by

$$\tau_{mix} = \left(\frac{L^2}{\varepsilon}\right)^{1/3}, \tag{4}$$

where L is the large eddy scale (set by the physical geometry of the fluid boundaries) and ε is the eddy dissipation rate. Complete mixing occurs in a few Corrsin timescales. Typical values for τ_{mix} are around 20–40 min for fairly vigorous boundary layer convection. A second timescale, which is more readily calcuable than τ_{mix} in the framework of the simulations presented in this study, is the large eddy turnover timescale τ_{eddy}, which can be approximated by $\tau_{eddy} = z_i/\sigma_w$. Parcels mix completely with their surroundings in a few large eddy mixing timescales. The large eddy timescales for our simulations are approximately 20 and 65 min for the strong and weak simulation cases, respectively. These values are similar to those calculated using τ_{mix}. Based upon the large eddy timescale we would conclude

TABLE 1. Details of trajectory ensembles used in this study.

Ensemble	N_{traj}	σ_w (m s^{-1})	τ_w (s)	z_b (m)	z_i (m)	$\overline{\tau}_{in,\infty}$ (min)	t_0 (min)
A	200	0.6	330	400	800	10	14
B	200	0.2	250	400	800	95	160

that the results of our TEM simulations are meaningful in the sense of being able to describe the evolution of the droplet size distribution to times of around 40–60 min in the strong turbulence cases and 120–180 min in the weak turbulence cases. Beyond these timescales the TEM ceases to be useful.

3. TEM model runs

Model runs were set up to examine the hypothesis that Ostwald ripening effects are important for the microphysical development of stratus/stratocumulus cloud. There is little dispute that Ostwald ripening would be an important factor in the microphysical development of a parcel that rose into cloud and then remained there for some hours (as in the simulations of CM99). It also seems clear, from the simulations of CM99, that vertical cycling motion *within* cloud is not necessary to obtain a ripening effect, and in fact does not enhance the effect at all. All that is required is that the parcel has sufficient time within the cloud. Stratus and stratocumulus clouds have a fundamentally different dynamical nature than the hypothetical clouds in the study CM99. Air parcels in stratus/stratocumulus are continually subject to rising and falling motion and any chosen parcel only has a finite in-cloud residence time. Once a parcel passes out of the cloud and into a subsaturated region, the effects of ripening on the size distribution of particles are rapidly lost. Therefore, it is important to consider the effects of parcels passing in and out of cloud in as realistic a manner as possible, in order to quantify ripening effects in stratus/stratocumulus. The mean in-cloud residence time ($\overline{\tau}_{in}$) is a useful parameter, and one would expect this to scale with the large eddy turnover time.

a. Trajectory ensembles and in-cloud residence times

Because the in-cloud residence time τ_{in} is a particularly important determinant of the propensity for Ostwald ripening, in this section we examine the statistics of in-cloud residence times for trajectories constructed using the transilient matrix approach. We compare two ensembles of trajectories; each ensemble represents conditions in a different boundary layer dynamic regime. Details of the two sets are given in Table 1. For each set the boundary layer depth was $z_i = 800$ m, with a cloud layer extending from a height of $z_b = 400$ m to the boundary layer top. Trajectory ensemble A is representative of parcel motions in a well-mixed boundary layer with fairly vigorous large convective cells: given by $\sigma_w = 0.6$ m s^{-1} and $\tau_w = 330$ s. The vertical wind power spectral peak [$kS(k)$] is found at a Lagrangian length scale of 500–600 m. These conditions are typical of a well-mixed stratocumulus-topped boundary layer (with a convective velocity scale $w_* \approx 0.75$–1.0 m s^{-1}). Observations of this type of stratform boundary layer cloud structure are numerous (e.g., Nicholls and Leighton 1986, flight 526). Ensemble B is also representative of conditions in a well-mixed boundary layer, but with a much weaker circulation. Dynamical parameters are $\sigma_w = 0.2$ m s^{-1}, $\tau_w = 250$ s, with a power spectral peak at a length scale of some 100–150 m. Conditions similar to these are more representative of a weakly turbulent stratus layer, one in which shear turbulent generation of turbulent kinetic energy (TKE) is more important than convective generation. Observations of this type of structure include Brost et al. (1982a,b), the 17 June 1976 flight.

Figure 1 shows several parameters derived from the ensemble of trajectories. For each trajectory that is in-cloud at some output time step we calculate the time τ_{in} since the parcel last entered cloud (the in-cloud residence time). The parameter $\overline{\tau}_{in}$ is the mean value of τ_{in} over all the trajectories at a particular time step. This is plotted for both ensembles as a function of time in Fig. 1a. The value of $\overline{\tau}_{in}$ rapidly reaches its equilibrium value for set A because there are very few trajectories that remain in cloud for longer than 50–60 min (Fig. 1c). However, this is not the case for ensemble B, for which $\overline{\tau}_{in}$ continues to increase for the entire 200 min of the simulation as a result of there being a significant number of parcels that remain in cloud for several hundred minutes (Fig. 1d). Figure 1b shows that the standard deviation of the in-cloud residence time is similar to the mean for both ensembles. This may prove to be useful in the parameterization of ripening effects in models without explicit bin microphysical representation. The pdf of in-cloud residence time at times 1, 2, and 3 h show that set A reaches an equilibrium within 1 h (i.e., the pdf's are the same at each time) whereas set B continues to shift to larger τ_{in} as the time progresses. The dotted curves in Fig. 1a, which match the simulated results well, take the form

$$\overline{\tau}_{in} = \overline{\tau}_{in,\infty}(1 - e^{-t/t_0}), \tag{5}$$

where $\overline{\tau}_{in,\infty}$ is the equilibrium ($t \to \infty$) value of $\overline{\tau}_{in}$ and t_0 is a time constant, where the values for $\overline{\tau}_{in,\infty}$ and t_0 are given in Table 1. Equation (5) is an empirical result, although it might be possible to derive an expression of this form from knowledge of the turbulent structure. It is clear that there is a large increase in the in-cloud residence time as the vertical wind standard deviation

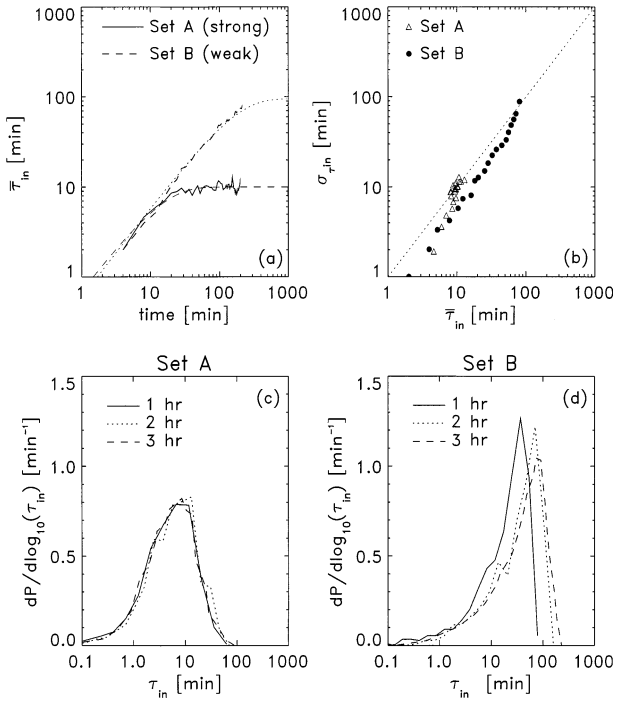

FIG. 1. (a) The mean time that a sampled parcel ($400 < z < 800$ m) has been in cloud, plotted as a function of time after the start of the simulation. The solid line (trajectory set A) is for the strong convective case; the dashed line (set B) is for the case of weaker circulations. The dotted lines are explained in the text. (b) Standard deviation of τ_{in} plotted as a function of the mean value. (c), (d) Probability density functions for τ_{in} derived for the (c) set A and (d) set B trajectories. Clearly, while there is little evolution of the set A residence time pdf, the set B pdf is evolving for the duration of the simulations.

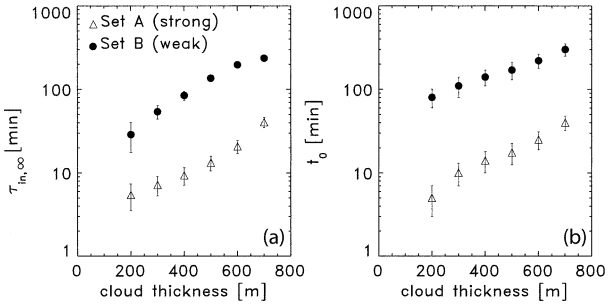

FIG. 2. Plot of (a) $\overline{\tau}_{in,\infty}$ and (b) t_0 [Eq. (5)] as a function of cloud thickness for trajectory sets A (triangles) and B (circles). The error bars show 95% confidence limits.

is reduced. We address the effect of this upon the cloud microphysics in the following section.

Figure 2 shows the effect of varying the cloud thickness upon the values of $\overline{\tau}_{in,\infty}$ and t_0. Both these variables increase markedly with increasing cloud thickness showing that the mean residence time at large t of a parcel within the cloud increases by around a factor of four as the cloud thickness doubles from 300 to 600 m. In addition, it is seen that $\overline{\tau}_{in,\infty}$ is approximately the same for a 700-m-thick strong circulation cloud as it is for a 200-m-thick weak circulation cloud. There is often a coupling between the turbulent dynamics and the thickness of a cloud so that $\tau_{in,\infty}$, t_0 and the cloud thickness are not truly independent parameters. We are aware that this exploration of ($\tau_{in,\infty}$, cloud thickness) phase space is idealized and may cover regions that do not occur in nature. However, the cloud thickness–dynamical coupling certainly does not result in a 1:1 mapping between these parameters, as there are many factors other than turbulent dynamics that determine boundary layer cloud thickness.

b. Description of microphysical TEM runs performed

In this paper we examine (i) weak and strong boundary layer circulations, and (ii) polluted and clean air mass types. Constant values of cloud-base height z_b = 400 m and cloud-top height z_i = 800 m are used. The surface pressure and temperature are 1012 hPa and 288.5 K, respectively. To investigate all combinations of (i) and (ii) above, we performed four simulations detailed in Table 2. Strong circulations were carried out using trajectory ensemble A (see previous section); weak circulations used ensemble B. Polluted air was simulated using an aerosol distribution consisting of ammonium sulphate in a lognormal distribution with mode radius of $r_{mode} = 0.04$ μm, a geometrical standard deviation of $\sigma_{geom} = 2.2$ and a concentration of $N_a = 1000$ cm^{-3}. Clean air masses were simulated using the same lognormal distribution but with a concentration N_a = 200 cm^{-3} (Fig. 3).

In the simulations presented here, the droplets are all assumed to follow parcel trajectories, which is certainly likely to be a valid assumption for small droplets. For example, the terminal velocities for droplets with radii 1, 5, and 15 μm are approximately 0.014, 0.32, and 2.7 cm s^{-1} respectively at the temperatures and pressures typical of atmospheric boundary layers. The times taken to fall 100 m (comparable to the large eddy size) for each of these droplets are 200, 8.7, and 1 h, respectively. It is reasonable then to expect droplets with radii smaller than 10–15 μm to remain on the trajectories. Droplets larger than this will tend to fall from their trajectories and a different modeling approach becomes necessary to describe them (Szumowski et al. 1999).

c. General features

Figure 4a shows the height–time series for sections of two trajectories (taken from set B). Both trajectories

TABLE 2. Details of simulation used in this study.

Simulation	Trajectory set [S (strong) or W (weak)?]	CCN [C (clean) or P (polluted)?]
SC	S	C
SP	S	P
WC	W	C
WP	W	P

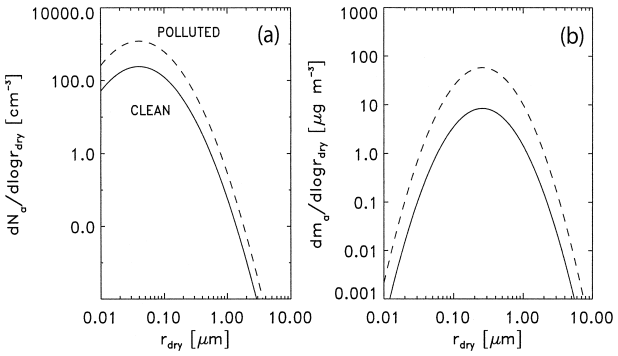

FIG. 3. (a) Aerosol number and (b) mass distributions used in this study. The polluted and clean modes are both modeled as lognormal distributions with number modal radius of 0.04 μm, geometrical standard deviation of 2.2, and number concentrations of 1000 cm^{-3} and 200 cm^{-3}, respectively.

show the parcel rising from cloud base to near the cloud top. The trajectory shown by the solid line takes considerably more time to reach the upper 100 m of the cloud than the one shown by the dashed line. The dotted line shows the height–time series for a parcel with a steady ascent rate equal to the mean ascent rate of the slow fluctuating parcel. The central panel shows the radii of droplets formed on two sizes of dry nucleus (r_{dry} = 0.05 μm—thin lines; r_{dry} = 0.6 μm—thick lines) as a function of height for the two trajectory sections. The critical radii of the two aerosol categories shown here are 0.48 and 20.1 μm, respectively. Thus, the larger of the two droplets never becomes activated (i.e., becomes larger than its critical radius) at any point in the ascent. The smaller of the two droplets is activated at all heights in cloud. Nevertheless the larger unactivated droplet gains mass at the expense of the smaller activated particle. This may in some senses seem counterintuitive. However, due to the curvature and salinity effects, the shape of the equilibrium supersaturation–droplet radius curve (''Kohler curve'') means that it is possible that large unactivated particles can grow at the same time as smaller activated particles are evaporating at the same supersaturation. Also shown in Fig. 4b are the droplet radii versus height from the steady slow updraft run (dotted lines), which demonstrates that the Ostwald ripening effect (large drop growing at the expense of the smaller) is taking place irrespective of the fluctuations in vertical ascent rate, a finding demonstrated clearly by CM99. The Fig. 4c shows the supersaturation against height for the steady updraft run.

Figure 5 shows the equilibrium supersaturation–droplet size curves for the two dry radii mentioned above. Note that in the shaded region, the unactivated droplet will grow and the activated one will evaporate. The history of the supersaturation within a parcel therefore is critical in determining whether $s < s_{eq}$ when $r > r_{crit}$ for a particular aerosol category (r_{crit} is the critical radius, i.e., the wet radius at which s_{eq} is a maximum for a particular dry aerosol). The supersaturation in which

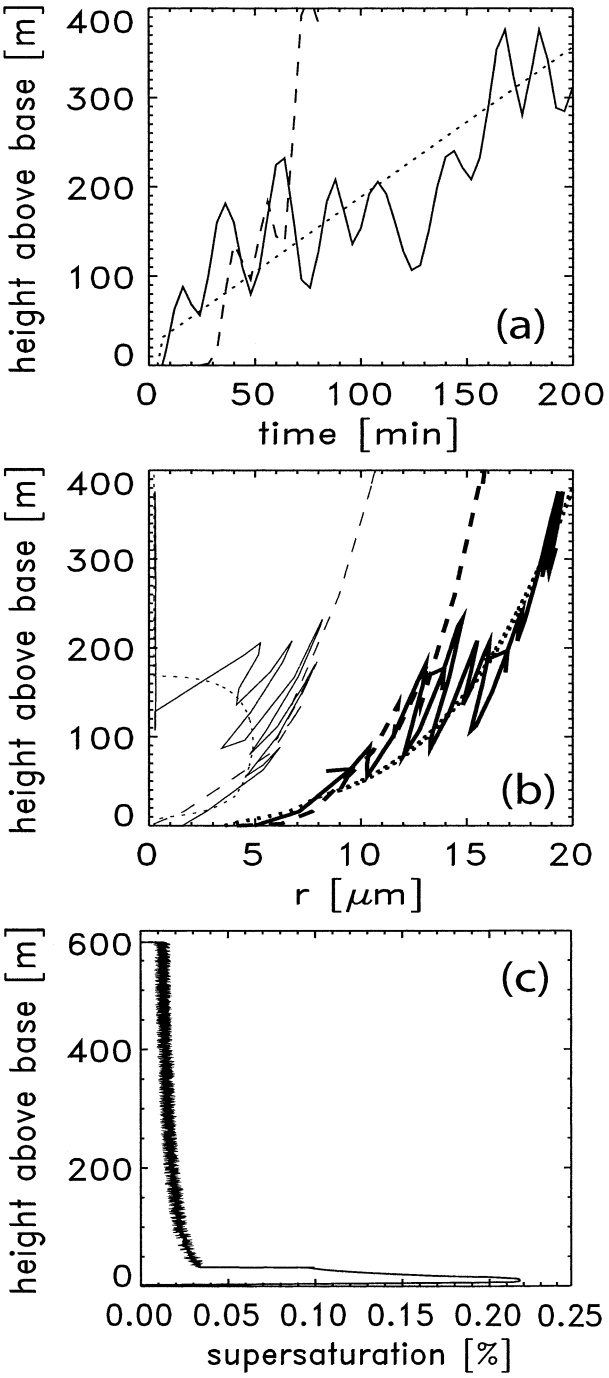

FIG. 4. Example of droplet growth in simulations with weak (solid lines) and strong (dashed lines) updrafts. (a) Height–time series for three example trajectories, one of which (dashed line) ascends more rapidly. The dotted line represents a steady ascent at the same mean ascent rate as the solid line. (b) The radii of droplets formed on two dry aerosol sizes (a = 0.05 μm, thin lines; a = 0.6 μm, thick lines). Large droplets have more time to grow, and small droplets more time to shrink, in the slowly ascending parcels, which results in broader size distributions at all heights in the cloud. The fluctuation in ascent rate in the nonsteady case is not a prerequisite for ripening to occur. (c) The supersaturation as a function of height from the steady ascent run.

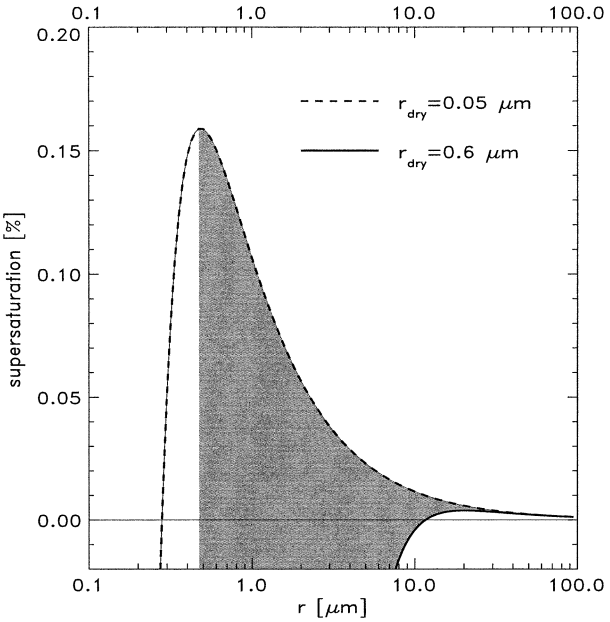

FIG. 5. Equilibrium supersaturation curves for dry ammonium sulfate particles with radii of 0.05 μm (dashed line) and 0.6 μm (solid line). The shaded area represents that part of the droplet radius–supersaturation phase space for which an activated $a = 0.05$ μm droplet will evaporate at the expense of an unactivated $a = 0.6$ μm droplet.

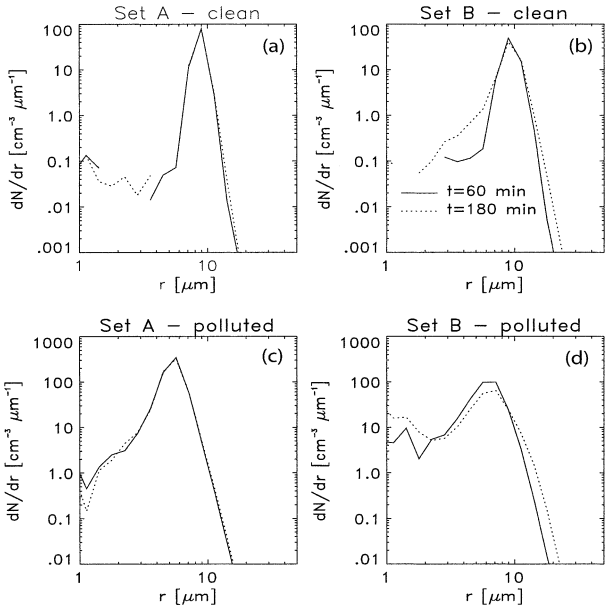

FIG. 6. Time evolution of the four droplet size distributions. The size distributions at 60 min (solid) and 180 min (dotted) after the start of the simulations are shown in each case. (a), (c) There is negligible evolution of the size distribution of droplets formed with trajectory set A; (b), (d) but those formed using set B continue to broaden with time toward both smaller and larger sizes. Data are all taken from the top half of the cloud ($600 < z < 800$ m).

a particular droplet finds itself is effectively decoupled from the activation of the droplet because of the presence of a spectrum of droplet sizes. Hence, it is possible for the supersaturation (which is controlled largely by the aerosol classes for which the mass growth is largest) to enter the shaded region of Fig. 5 and therefore it is possible for a particular droplet to deactivate once it has been activated.

In all rising parcels with physically realistic updraft speeds and aerosol size distributions, it can be shown that the rate of decrease of supersaturation after the initial sharp peak (e.g., higher than 50 m above cloud base in Fig. 4c) is slow, taking several thousand seconds to fall from 1/10 to 1/20 of the peak supersaturation. The simulations of CM99 show a similarly slow decay time for supersaturation. Their parcel was allowed to rise from just below cloud base for 20 min. Following the ascent the vertical wind speed was reduced to zero. The peak supersaturation was approximately 0.34% and fell to around 0.03% in approximately 20 min. However, it took around 3 further hours for the supersaturation to fall to 0.015%. This slow decay of supersaturation, which appears to be a feature of all parcel model ascents, allows the Ostwald ripening process to occur over long periods of time.

d. Droplet size distributions

Figure 6 shows droplet size distributions from the trajectory ensemble model at two different times (60 and 180 min) after the start of the simulations. Each size distribution is averaged over the top 200 m of the cloud layer ($600 < z < 800$ m). Simulations generated using trajecory set A (Figs. 6a and 6c) are clearly less dispersive than those generated using the weak circulation set B (Figs. 6b and 6d). Dispersion is defined as the ratio of the standard deviation of drop radii to the mean radius. The difference in dispersion between the weak and the strong circulations is more marked in the clean aerosol case. There is clearly very little evolution of any of the size distributions from simulations using trajectory set A. Significantly more evolution is seen in the trajectory set B simulations, which results from the longer in-cloud residence time for parcels in this set.

Because the size distributions presented are averaged over 200 m of height, it is useful to know how much width in the size distribution is caused by averaging over this range. Because there is little variation of the droplet concentration with height, this source of dispersion arises almost entirely from variations in liquid water content among the contributing parcels. For example, a parcel at $z = 600$ m, has a liquid water content equal to around half that at $z = 800$ m. In this case the spectral dispersion caused by variations in liquid water content within the 200-m-thick averaging layer is approximately 0.06. This is considerably smaller than the dispersion caused by physical processes (rather than height averaging) in all cases.

It is found that the concentration N_d of droplets with radii larger than 1 μm is always close to the concentration of activated particles. There is little evidence for

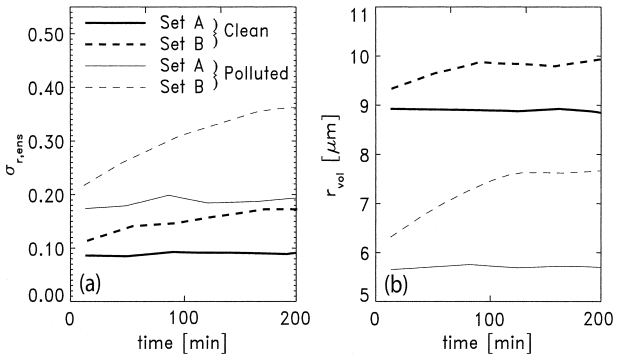

FIG. 7. Time evolution of (a) the radius dispersion $\sigma_{r,\mathrm{ens}}$ of the averaged size distribution ($600 < z < 800$ m) and (b) the mean volume radius r_{vol} for the four cases with no giant CCN. Polluted cases (thin lines) show generally broader size distributions (larger dispersions) than the clean cases (thick lines). Set B cases are generally broader and show considerable time evolution. The clean cases have larger values of r_{vol} throughout the simulations. The value of r_{vol} increases in the set B simulations reflecting the decrease in activated droplet concentration with time.

ripening of the set A droplet size distributions with time after approximately 50 min into the simulations, but with set B simulations there is a fall in droplet concentration, a rise in $r > 20$ μm particles and a rise in the number of unactivated aerosol over the course of 200 min. This ripening effect is present in both the clean and the polluted simulations.

The result demonstrating only time evolution of parameters derived from set B simulations is consistent with the in-cloud residence time probability distributions (Fig. 1). For weak circulations (set B), this pdf does not equilibrate until well after the 200 simulation minutes (demonstrated by generating extended trajectories). The microphysical results have little meaning at such long timescales and so we cannot present meaningful parcel model results at these long timescales. For strong circulations (set A) the in-cloud residence time pdf equilibrates in less than 1 h which explains the lack of time evolution of spectral characteristics.

Figure 7 shows the spectral dispersion and mean volume radii as a function of time. All data are taken from the averaged (ensemble) size distributions ($600 < z < 800$ m). Set A simulations show little change with time in either of these parameters, whereas the set B volume radii increase with time as the size distributions broaden and the droplet number concentration falls. The timescales for evolution of the volume radius and the spectral dispersion are similar. In terms of the largest fractional change in volume radius (or equivalently, droplet concentration), the polluted case shows a greater degree of Ostwald ripening than the clean case. This is in accordance with what would be expected from Eq. (3).

e. Comparison with single parcel ascent

To investigate the effects of parcel circulation and in-cloud residence time we compare the TEM results with a single parcel, initialized below cloud base, and rising into the cloud with a vertical ascent rate equal to the standard deviation of the vertical wind from the corresponding TEM trajectory set. This ascent rate is chosen because it represents a measure of the typical strength of the updrafts in the cloud layer.

Table 3 shows the mean droplet number concentration (concentration with radii larger than 1 μm), mean volume radius r_{vol} and dispersion, calculated from the TEM and the single parcel ascent. In each case the data are taken from the height region $600 < z < 800$ m. The TEM results are taken between times 120 and 180 min after the start of the simulations so that much of the Ostwald ripening will have taken place. In all cases the single parcel model produces size distributions with lower dispersions than the TEM. However, for the strong circulations, the ratio of the TEM dispersion to the single parcel dispersion is approximately 1.2, while for the weak circulations the ratio ranges from 1.6 to 2.1. In all set B cases, the single parcel dispersions are close to those in the TEM near the start of the simulations (see Fig. 7), showing that the TEM and single parcel models dispersion differences in Table 3 are mainly a result of the time development (i.e., ripening) of the TEM size distributions.

The number concentrations and volume radii do not markedly differ between the TEM and single parcel methods, which suggests that the increased TEM dispersion in the weak circulation cases is largely caused by a broadening both to small and larger sizes. This is clearly demonstrated in Fig. 8, which shows the TEM and single parcel droplet size distributions from which the data in Table 3 were derived. In all size distributions the single parcel model results in very few droplets smaller than 3 μm. The time evolution of the TEM size distributions (Fig. 6) demonstrate that broadening to small sizes takes place over long timescales with set B

TABLE 3. Comparison between parcel model approaches. Data for TEM and single parcel simulations are averaged over the height range $600 < z < 800$ m, for TEM values, averages are taken over times 120–180 min after the start of simulations.

	N_d (cm^{-3})		r_{vol} (μm)		Dispersion	
Simulation	TEM	Single	TEM	Single	TEM	Single
SC	196	163	8.90	9.28	0.092	0.075
SP	763	683	5.72	5.76	0.190	0.155
WC	148	113	9.84	10.48	0.166	0.106
WP	348	339	7.70	7.27	0.335	0.163

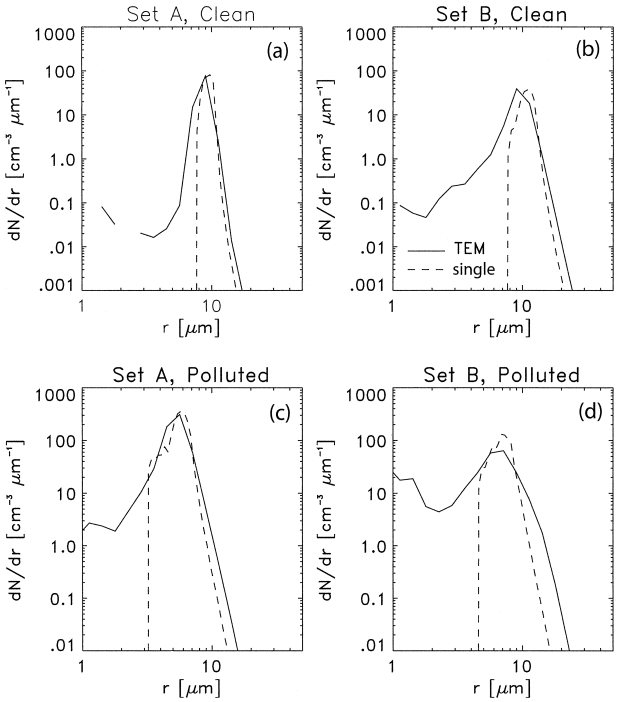

FIG. 8. Comparison of trajectory ensemble model (TEM, solid lines) and single parcel model (dashed lines) drop size distributions for (a), (b) clean and (c), (d) polluted conditions. In all cases, but particularly for the comparison with the TEM weak trajectories, the single parcel model produces considerably narrower distributions and an absence of the smallest droplets.

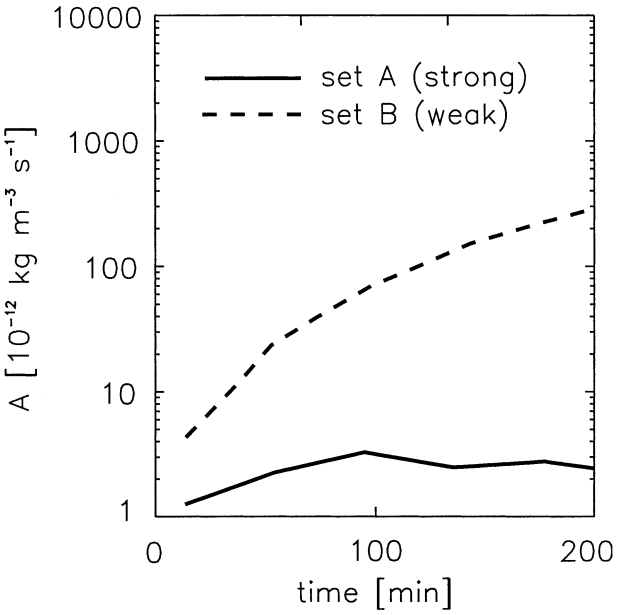

FIG. 9. Autoconversion rates as a function of time calculated from TEM model distributions for clean simulations. Autoconversion is higher for the weak circulations (dashed line) and increases with time during the 200 min shown. The autoconversion rate in the weak case is almost two orders of magnitude larger than in the strong case (solid line) after 2 h.

trajectories due to the long in-cloud residence times of some of the parcels. However, in all TEM simulations there are considerably more small droplets ($r < 3$–4 μm) than there are in the single parcel simulations. Clearly then, some of the higher numbers of small droplets in the TEM are not the result of Ostwald ripening alone since set A simulations experience hardly any size distribution changes at all after 1 h. The presence of these droplets is likely to be the result of deactivation and reactivation of droplets as the vertical wind changes from negative to positive.

4. Effect upon autoconversion of cloud droplets

From the model droplet size distributions it is possible to compute estimates of the autoconversion of cloud liquid water to drizzle liquid water. We do not include these effects in the parcel simulations themselves; we use offline calculations merely to show the *potential* for drizzle formation. Here, we use the method of Austin et al. (1995b) to calculate the rate of mass transfer of drops across the $r = 20$ μm boundary. The droplet size distribution between $1 < r < 20$ μm is obtained from the trajectory ensemble model parcels, and binned onto 60 bins, logarithmically spaced in r. For this example we use the mean size distributions in the layer $600 < z < 800$ m derived as a function of time, although it would be possible to use any height interval one wished. We solve the stochastic collection equation using the computationally efficient code of Bott (1998), which can be carried out with minimal numerical diffusion using time steps equal to 10 s. As in Austin et al. (1995b) we define the autoconversion A as the mass transfer rate across the $r = 20$ μm boundary over 10 min. This is appropriate because the mass transfer rate is close to constant over the 10-min period. Collection efficiencies are taken from Hall (1980).

Figure 9 shows the autoconversion calculated from the model size distributions for the clean cases. Simulations with trajectory sets A and B initially start with similar autoconversion rates but due to ripening effects in set B, the autoconversion increases rapidly. After 2 h (Fig. 9) the set B autoconversion rate is almost two orders of magnitude larger than for the set A distributions. This suggests that the effects of spectral ripening (in boundary layer clouds with weak circulations) are integral to the initial production of drizzle in stratiform boundary layer clouds and as such may need to be addressed when deriving parameterizations for use in large-scale models.

5. Discussion

In this study we have used an ensemble of parcels moving within a well-mixed cloud-topped boundary layer in an attempt to assess the potential importance of size distribution changes due to temporal Ostwald ripening. CM99

showed that ripening broadens the droplet size distribution within a single closed parcel. This occurs due to a thermodynamic instability, which means that large drops tend to grow at the expense of smaller ones leading to a broadening of the droplet size distribution over time *without* the need for supersaturation fluctuations. In turbulent boundary layer clouds the supersaturation does fluctuate. We have demonstrated that the ripening effect occurs only in clouds where the parcel in-cloud lifetimes are sufficiently large for the Ostwald ripening process to occur. A ripening timescale within parcels remaining stationary within a cloud after an initial rise into the cloud is a function of the nature of the dynamics and the aerosol's physical and chemical properties. For example, simulations show that higher aerosol concentrations result in a greater degree of Ostwald ripening given fixed dynamics. It is difficult to define the ripening timescale formally but the process is ultimately controlled by the rate of decay of supersaturation within the parcel. This process tends to occur over timescales of several hours, and results in broader (more dispersive) size distributions with lower droplet concentrations.

The trajectory ensemble has been used to examine the statistics of in-cloud residence time for two sets of trajectories: the first set is typical of fairly vigorous thermals, which are typical of convectively driven stratocumulus clouds. The second set is more characteristic of weaker stratus clouds formed through cooling of an airmass from below or in relatively high wind speed conditions. The distributions of in-cloud residence time for a 400-m-thick cloud shows that there are few parcels in the vigorous case that are in cloud for more than 50–60 min. However, for the weak case a significant proportion of the parcels remain in cloud for over an hour, and some remain in cloud for considerably longer. It is also noted therefore that parcel model ensembles, in which some parameters depend strongly upon in-cloud residence time, could require several hours of integration before equilbrium is reached. This could be particularly important in studies of both aqueous-phase and gas-droplet chemistry and cloud processing of aerosols, and the interaction of droplets with radiation.

We found, for the cases with long in-cloud residence times, the the size distribution continued to broaden to both small and large sizes for the entire 200-min simulation. The droplet concentration ($r > 1$ μm) falls with time and the number of unactivated particles rises as droplets are deactivated due to the Ostwald ripening process. The number of droplets with radii larger than 20 μm increases, in both the clean and polluted cases. Autoconversion rates were found to increase in all the weak circulation cases. In contrast, negligible time evolution of parameters is seen in any of the strong circulation cases. These results show that to accurately model the droplet size distribution in weakly turbulent boundary layer clouds, it may be necessary to account for the possible slow microphysical temporal evolution. In addition, the response of cloud layers to changes in their turbulent structure can in some cases be particularly slow, with clouds possessing long microphysical memories of previous dynamical structure.

Upon examining the microphysical evolution during ascent, it is apparent that the only requirement for the ripening process to occur is time. Thus, a parcel with a slow ascent will take longer to reach a particular level and will therefore have had more ripening time. Fluctuations in ascent rate have little effect per se, but they are likely to cause a parcel to remain in cloud for longer.

The simulations presented in this study did not include the effects of entrainment, radiative growth, or parcel–parcel mixing. Stevens et al. (1996) find that entrainment across cloud top is a large source for size distribution dispersion. However, it is not known how entrainment will affect the results presented here, in terms of the ripening of size distributions with time. It will be an interesting study to carry out using TEM with LES-derived trajectories, which can include the effects of entrainment mixing. Radiative growth may well increase the temporal evolution effects because large droplets will grow in parcels with long cloud-top residence times. Parcel–parcel mixing is impossible to simulate using the TEM framework presented here. As Korolev (1995) points out, a parcel is likely to undergo mixing with the cloud environment within a relatively short time. Whether parcel–parcel mixing leads to more or less ripening of the droplet size distribution is a subject for future research. It might be possible to simulate effects of parcel–parcel mixing using a two-dimensional size distribution (Bott 2000), which allows binning of the droplet size distribution without losing information about the CCN within the droplets.

Acknowledgments. We are grateful to colleagues in the Met Office, particularly at the Met Research Flight, for discussions that aided the research presented in this paper. Sarah Irons was supported by a Natural Environment Research Council Ph.D. scholarship. We would like to thank Philip Austin and two anonymous reviewers for their constructive comments and suggestions, which improved the final manuscript.

APPENDIX

Simulation of Turbulent Parcel Motion

Calculation of the transilient matrix elements for very small vertical grid spacings is computationally prohibitive [the number of operations scale, approximately, with the square of the number of levels used because (a) there is a cubic relationship between the number of operations required for square matrix multiplication and the number of levels and (b) the number of multiplications required decreases approximately linearly with the number of levels]. We found that computation of the transilient matrix was readily possible for grid spacings of 5–10 m (with 100 levels). The standard deviation

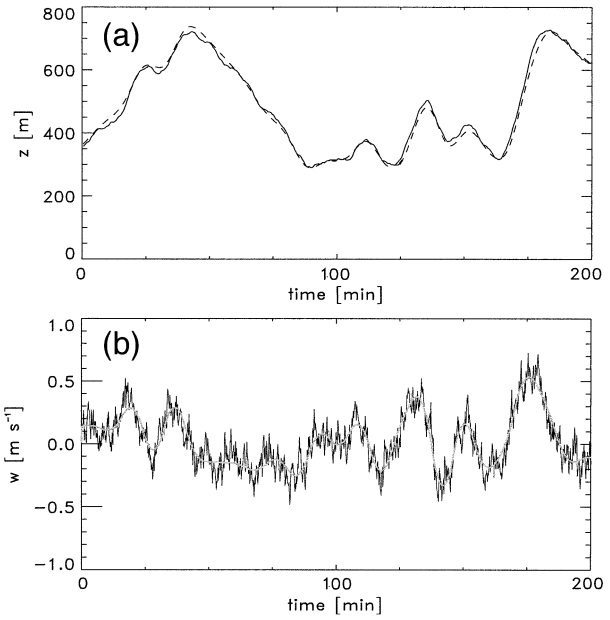

FIG. A1. (a) Time series of parcel height and (b) ascent rate for an example parcel taken from trajectory set B (weak circulation). In (a), the solid line includes the effects of small-scale turbulence; the dashed line does not. In (b), the black line includes the small-scale turbulent fluctuations; the gray line does not.

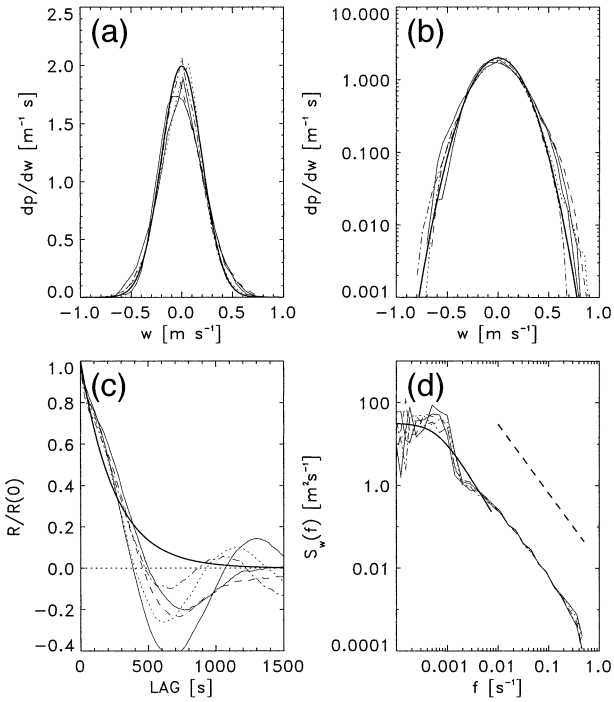

FIG. A2. Example of trajectory diagnostics for the weak circulation case (set B). (a), (b) Vertical wind pdf's [using (a) linear and (b) logarithmic ordinate]. Five trajectories are shown here. The thick solid line shows the Gaussian distribution with standard deviation σ_w = 0.2 m s^{-2}. (c) The normalized Lagrangian autocorrelation function of the parcel ascent rate (vertical wind). The thick solid line is explained in the text. (d) The vertical wind power spectral density. The thick dashed line exhibits Kolmogorov ("$-5/3$") scaling. The thick solid line is described in the text.

in vertical wind speed in stratus and stratocumulus clouds is usually within the range of $0.2 < \sigma_w < 0.8$ m s^{-1}. In order to generate realistic physical behavior of the trajectory dynamics, a transilient matrix time step δt_{trans} should be chosen to be long enough so that there is a reasonable possibility that parcels can jump at least one level per time step. In this study, we chose $\delta t_{\text{trans}} =$ 240 s so that even trajectories for the lowest σ_w would satisfy this condition.

It is clear that real atmospheric trajectories in turbulent boundary layers will be subject to considerable fluctuations in ascent rate on timescales shorter than δt_{trans}. We added fluctuations on all timescales between δt_{trans} and δt_{micro} using a bounded additive cascade model (Marshak et al. 1994; Cahalan et al. 1994). This model leads to a power spectrum which exhibits Kolmogorov scaling [i.e., the power spectral density of the vertical wind along the Lagrangian trajectory is proportional to (frequency)$^{-5/3}$]. To achieve this, the vertical wind time series along a trajectory was derived from the height–time series. This series was converted to a time series with spacing δt_{micro} using a cubic spline interpolator. Short sections of turbulent time series (each with total time δt_{trans} and time step δt_{micro}; i.e., 240/0.1 = 2400 data points) with zero mean were generated using the cascade model and added back-to-back to the spline-interpolated trajectory series. The total variance contained in timescales shorter than δt_{trans} was chosen to match the power observed in the trajectory-derived vertical wind at δt_{trans}. Finally, the ($1/\delta t_{\text{micro}}$ Hz) height–time series for the trajectory was calculated by integration of the vertical wind time series.

Time series for an example trajectory is shown in Fig. A1. The upper panel shows the trajectory height as a function of time for the case where no small-scale turbulence is added (dashed) and when turbulence is added (solid). The bottom panel shows the vertical parcel speed as a function of time for the case of no turbulence (gray line) and with turbulence (solid black).

To assess the physical realism of the resulting trajectories we calculated pdf's, autocorrelation functions, and power spectra of the vertical wind. Figure A2 shows pdf's of w plotted using (a) linear and (b) logarithmic ordinates (five example trajectories are shown). All trajectories were calculated with τ_w = 250s, and σ_w = 0.2 m s^{-1}. In each case, the pdf of the vertical wind speed demonstrates near-Gaussian behavior (shown by the thick solid line), as expected. Normalized Lagrangian autocorrelation functions $R/R(0)$ and Lagrangian power spectra are shown in Figs. A2c and A2d, respectively. The solid line in Fig. A2c is the autoconversion function

$$R(r) = \sigma_w^2 \exp(-|r|/\lambda_w), \qquad \text{(A1)}$$

which corresponds to the idealized power spectrum used

to derive the elements of the transilient matrix (Austin et al. 1995b); that is,

$$S(k) = \frac{2}{\pi}\left(\frac{\sigma_w^3 \tau_w}{1 + \sigma_w^2 \tau_w^2 k^2}\right), \qquad \text{(A2)}$$

where $\lambda_w (= \sigma_w \tau_w)$ is the Eulerian integral lengthscale, r is the lag distance, and k is the wavenumber. Autocorrelation functions and power spectra calculated from the simulated trajectories should match those given by Eqs. (A1) and (A2), respectively, if the Eulerian and Lagrangian integral scales are approximately equal. If we make this assumption, then it can be seen from Figs. A2c,d that the agreement between simulated and idealized spectra is reasonably good. Lenschow and Stankov (1986) demonstrate that the idealized autocorrelation functions, almost identical in form (at wavenumbers around and smaller than the spectral peak) to those above, match quite well with observations of power spectra in convective boundary layers. This gives us some confidence that the simulated trajectories in this study are representing realistic boundary layer motions.

The spline interpolation was found to lead to very little power at timescales larger than δt_{trans}. Without the addition of the small-scale turbulent motions (i.e., with only the effect of the spline interpolation to provide power), the vertical wind power spectra contain at least two orders of magnitude less power at frequencies greater than approximately $1/\delta t_{\text{trans}}$. This is the case even when only very low levels of small-scale turbulence was added to the transilient trajectories.

REFERENCES

Austin, P., S. Siems, and Y. Wang, 1995a: Constraints on droplet growth in radiatively cooled stratocumulus clouds. *J. Geophys. Res.,* **100,** 14 231–14 242.

——, Y. Wang, R. Pincus, and V. Kujala, 1995b: Precipitation in stratocumulus clouds: Observational and modeling results. *J. Atmos. Sci.,* **52,** 2329–2352.

Bartlett, J. T., and P. R. Jonas, 1972: On the dispersion of the sizes of droplets growing by condensation in turbulent clouds. *Quart. J. Roy. Meteor. Soc.,* **98,** 150–164.

Baumgardner, D., W. Strapp, and J. E. Dye, 1985: Evaluation of the forward scattering spectrometer probe. Part II: Corrections for coincidence and dead-time losses. *J. Atmos. Oceanic Technol.,* **2,** 626–632.

Beard, K. V., and H. T. Ochs III, 1993: Warm-rain initiation: An overview of microphysical mechanisms. *J. Appl. Meteor.,* **32,** 608–625.

Bott, A., 1998: A flux method for the numerical solution of the stochastic collection equation. *J. Atmos. Sci.,* **55,** 2284–2293.

——, 2000: A flux method for the numerical solution of the stochastic collection equation: Extension to two-dimensional particle distributions. *J. Atmos. Sci.,* **57,** 284–295.

Brenguier, J.-L., and L. Chaumat, 2001: Droplet spectral broadening in cumulus clouds. Part I: Broadening in adiabatic cores. *J. Atmos. Sci.,* **58,** 628–641.

——, T. Bourrianne, A. De Araujo Coelho, J. Isbert, R. Paytavi, D. Trevarin, and P. Weschler, 1998: Improvements of droplet size distribution measurements with the Fast-FSSP (Forward Scattering Spectrometer Probe). *J. Atmos. Oceanic Technol.,* **15,** 1077–1090.

Brost, R. A., D. H. Lenschow, and J. C. Wyngaard, 1982a: Marine stratocumulus layers. Part I: Mean conditions. *J. Atmos. Sci.,* **39,** 800–817.

——, J. C. Wyngaard, and D. H. Lenschow, 1982b: Marine stratocumulus layers. Part II: Turbulence budgets. *J. Atmos. Sci.,* **39,** 818–836.

Cahalan, R. F., W. Ridgway, W. J. Wiscombe, T. L. Bell, and J. B. Snider, 1994: The albedo of fractal stratocumulus clouds. *J. Atmos. Sci.,* **51,** 2434–2455.

Celik, F., and J. D. Marwitz, 1999: Droplet spectral broadening by ripening process. Part I: Roles of curvature and salinity of cloud droplets. *J. Atmos. Sci.,* **56,** 3091–3105.

De Baas, A. F., H. van Dop, and F. T. M. Nieuwstadt, 1986: An application of the Langevin equation for inhomogeneous conditions to dispersion in a convective boundary layer. *Quart. J. Roy. Meteor. Soc.,* **112,** 165–180.

Dye, J. E., and D. Baumgardner, 1984: Evaluation of the Forward Scattering Spectrometer Probe. Part I: Electronic and optical studies. *J. Atmos. Oceanic Technol.,* **1,** 329–344.

Fitzgerald, J. W., 1972: A study of the initial phase of cloud droplet growth by condensation: Comparison between theory and observation. Ph.D. dissertation, Dept. of Geophysical Science, University of Chicago, 144 pp.

Fukuta, N., and L. A. Walter, 1970: Kinetics of hydrometeor growth from a vapor-spherical model. *J. Atmos. Sci.,* **27,** 1160–1172.

Hall, W. D., 1980: A detailed microphysical model within a two-dimensional dynamic framework: Model description and preliminary results. *J. Atmos. Sci.,* **37,** 2486–2507.

Harrington, J. Y., G. Feingold, and W. R. Cotton, 2000: Radiative impacts on the growth of a population of drops within simulated summertime Arctic stratus. *J. Atmos. Sci.,* **57,** 766–785.

Howell, W. E., 1949: The growth of cloud drops in uniformly cooled air. *J. Meteor.,* **6,** 134–149.

Korololev, A. V., 1995: Effect of supersaturation fluctuations on droplet size spectra formation. *J. Atmos. Sci.,* **52,** 3620–3634.

Lenschow, D. H., and B. B. Stankov, 1986: Length scales in the convective boundary layer. *J. Atmos. Sci.,* **43,** 1198–1209.

Marshak, A., A. Davis, R. F. Cahalan, and W. J. Wiscombe, 1994: Bounded cascade models as non-stationary multifractals. *Phys. Rev.,* **E49,** 55–79.

Nicholls, S., 1987: A model of drizzle growth in warm, turbulent, stratiform clouds. *Quart. J. Roy. Meteor. Soc.,* **113,** 1141–1170.

——, and J. Leighton, 1986: An observational study of the structure of stratiform cloud sheets: Part I. Structure. *Quart. J. Roy. Meteor. Soc.,* **112,** 431–460.

Pruppacher, H. R., and J. D. Klett, 1997: *Microphysics of Clouds and Precipitation.* 2d ed. Kluwer Academic, 994 pp.

Srivastava, R. C., 1991: Growth of cloud drops by condensation: Effect of surface tension on the dispersion of drop sizes. *J. Atmos. Sci.,* **48,** 1596–1605.

Stephens, G. L., 1978: Radiation profiles in extended water clouds. I: Theory. *J. Atmos. Sci.,* **35,** 2111–2122.

Stevens, B., G. Feingold, W. R. Cotton, and R. L. Walko, 1996: Elements of the microphysical structure of numerically simulated nonprecipitating stratocumulus. *J. Atmos. Sci.,* **53,** 980–1006.

Stull, R. B., 1984: Transilient turbulence theory. Part I: The concept of eddy mixing across finite differences. *J. Atmos. Sci.,* **41,** 3351–3367.

Szumowski, M. J., R. M. Rauber, and H. T. Ochs III, 1999: The microphysical structure and evolution of Hawaiian rainband clouds. Part III: A test of the ultragiant nuclei hypothesis. *J. Atmos. Sci.,* **56,** 1980–2003.

Tang, I. N., and H. R. Munkelwitz, 1994: Water activities, densities, and refractive indices of aqueous sulphates and sodium nitrate droplets of atmospheric importance. *J. Geophys. Res.,* **99,** 18 801–18 808.

Wendisch, M., A. Keil, and A. V. Korolev, 1996: FSSP characterization with monodisperse water droplets. *J. Atmos. Oceanic Technol.,* **13,** 1152–1165.